Supplement of Earth Syst. Dynam., 16, 565–583, 2025
https://doi.org/10.5194/esd-16-565-2025-supplement

Earth System Dynamics
Open Access
EGU

Supplement of

High probability of triggering climate tipping points under current policies modestly amplified by Amazon dieback and permafrost thaw

Jakob Deutloff et al.

Correspondence to: Jakob Deutloff (jakob.deutloff@uni-hamburg.de)

S1 Timestepping Scheme

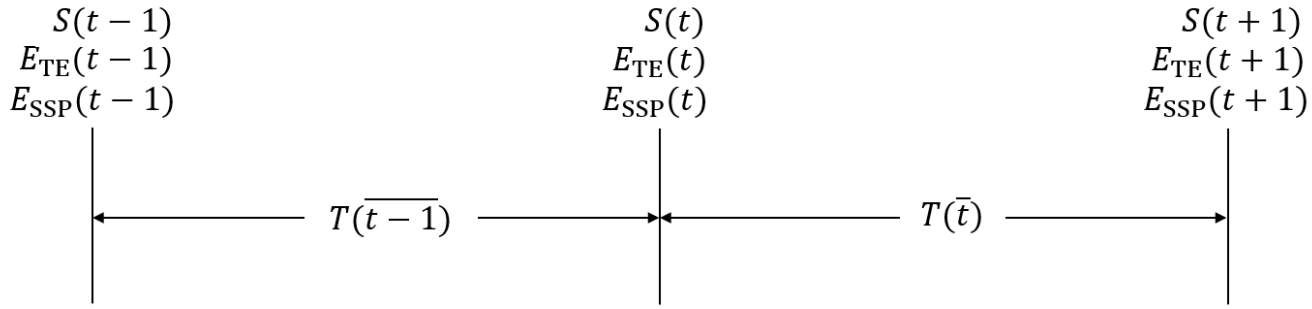

Figure S1. Schematic representation of the timestepping scheme in FaIR. Vertical lines represent single timesteps and horizontal arrows the time between them. Variables should be interpreted as single values given at a time step (over vertical lines), or as averages between the timesteps (between vertical lines).

S2 Derivation of CTEM Formulation

To derive the discrete form of CTEM, we start by rewriting the logistic equation for S

$$\frac{dS}{dt} = r\frac{T}{P}S - \frac{rT}{PK}S^2 \tag{S1}$$

We simplify this equation by defining a and b as

$$a := r\frac{T}{P} \tag{S2}$$

$$b := \frac{rT}{PK}. \tag{S3}$$

With those definitions, we can rewrite eq. S1 as

$$\frac{dS}{dt} = aS - bS^2. \tag{S4}$$

We further define

$$u := S^{-1}, \tag{S5}$$

which gives us

$$S = u^{-1},$$
$$\frac{dS}{du} = -u^{-2}\frac{du}{dt},$$

with which we can rewrite eq. S4 as

$$-u^{-2}\frac{du}{dt} = au^{-1} - bu^{-2}. \tag{S6}$$

We multiply eq. S6 with $-u^2$ and rearrange which gives us

$$\frac{du}{dt} + au = b. \tag{S7}$$

As eq. S7 is a Bernoulli differential equation, we know that an exact solution exists, which can be derived analytically. Since output variables from FaIR such as T are treated as constant between timesteps, this also holds for a and b which are calculated using eq. S2 and eq, S3 with $T = T(\overline{t-1})$. Hence, eq. S7 is a Bernoulli differential equation with constant coefficients which can be solved with an integrating factor I defined as

$$I := e^{at}.$$

We now multiply eq. S7 with I which yields

$$e^{at}\frac{du}{dt} + e^{at}au = be^{at}.$$

This equation is now integrated from $t-1$ to t to give the new solution for u at t

$$\int_{t-1}^{t} e^{at'} \frac{du}{dt'} + e^{at'} au \, dt' = \int_{t-1}^{t} be^{at'} \, dt'.$$

The left-hand integral can now be solved using the chain rule

$$\left[e^{at'} u\right]_{t-1}^{t} = b \int_{t-1}^{t} e^{at'} \, dt'.$$

The right-hand integral can be solved directly, and we derive

$$e^{at} U_2 - e^{a(t-1)} U_1 = \frac{b}{a} \left(e^{at} - e^{a(t-1)}\right).$$

Here, u is a function of t but to prevent confusion of brackets, we write U_2 for $u(t)$ and U_1 for $u(t-1)$. We simplify this equation by dividing by e^{at} and defining $\Delta t := t - (t-1)$

$$U_2 - e^{-a\Delta t} U_1 = \frac{a}{b} \left(1 - e^{-a\Delta t}\right).$$

Now, we resubstitute for u using eq. S5

$$S_2^{-1} - e^{-a\Delta t} S_1^{-1} = \frac{b}{a} \left(1 - e^{-a\Delta t}\right),$$

which can be rewritten as

$$S_2 = \left(e^{-a\Delta t} \left(S_1^{-1} - \frac{b}{a}\right) + \frac{b}{a}\right)^{-1}.$$

Explicitly showing the time dependency of S, b and a, we derive

$$S(t) = \left(e^{-a(\overline{t-1})\Delta t} \left(S^{-1}(t-1) - \frac{b(\overline{t-1})}{a(\overline{t-1})}\right) + \frac{b(\overline{t-1})}{a(\overline{t-1})}\right)^{-1}.$$

Bars over t denote that the respective variable is treated as the average value between two gridpoints, whereas variables without a bar over t are defined at the gridpoints (Fig. S1).

S3 Calibration of CTEM

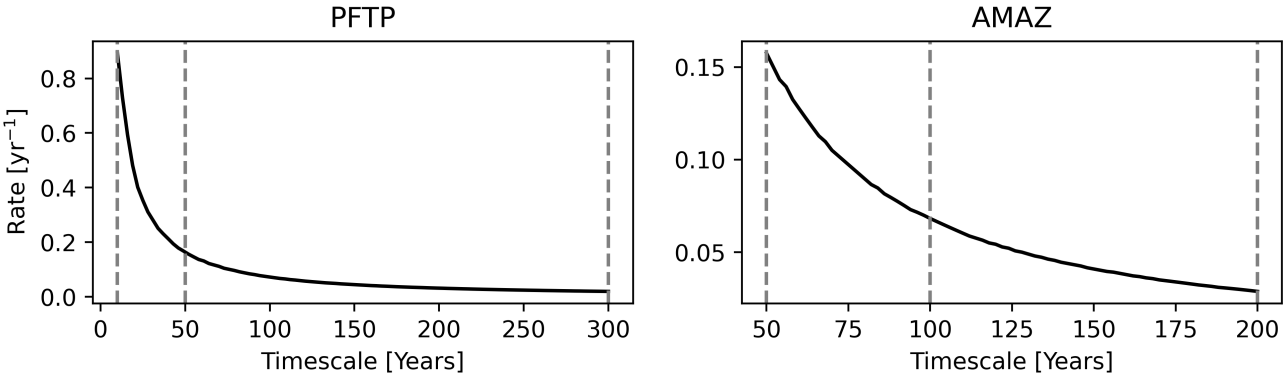

Figure S2. Calibrated rate (r) for H of PFTP and AMAZ. Grey vertical lines denote maximum, mean and minimum estimate of H from Tab. 1.

For the definition of S_0, we define the tipping timescale as the period over which 99% of the cumulative carbon emissions occur, which means S_0 is defined as 0.5% of K ($K_{\max}$ for PFAT). All calibrations of r are performed under the SSP5-8.5 scenario, as most model studies which inform the emission estimates of all three TEs were performed under the corresponding RCP8.5 scenario (Armstrong McKay et al., 2022). To increase transparency, all TEs are calibrated individually, with the other two TEs being deactivated. Furthermore, we use the default parameterization of FaIR for all calibrations.

For the calibration of PFTP and AMAZ, we use the respective mean estimate for P and K. We calibrate r by splitting the respective range of H from Tab. 1 into ~ 100 equally spaced bins, with one value of r fitted to each bin. We define the following objective function, which resembles the squared difference (D) between the observed H of the model and the expected value:

$$D = ((Y_{\text{end}} - Y_{\text{start}}) - H)^2, \tag{S8}$$

with Y_{end} being the year in which 99.5% of maximum cumulative emissions are emitted and Y_{start} the year in which the respective TE is triggered. These values are looked up in the model results without any further time-aggregation being necessary, which increases the performance of the calibration algorithm. The objective function is minimized for each bin of H for AMAZ and PFTP using the Nealder-Mead algorithm (Gao and Han, 2012), which gives the calibrated values of r (Fig. S2). The objective function has been successfully minimized to zero for all bins of H for PFTP and AMAZ.

For PFAT, we only calibrate r for the mean estimate of H, using the mean values of P and $K_{\max}$ with $K = K_{\max}$ at all times. This is due to the fact that the timescale over which the emissions from PFAT occur is already included in the ranges of F_{100} and F_{300}. The value of $r = 0.041\ \text{yr}^{-1}$ corresponding to the mean value of $H = 200$ years is determined by using the objective function (eq. S8), which is minimized to zero.

S4 Test of CTEM Calibration

Here, we investigate how well the calibrated version of CTEM resembles the estimated values of H of PFTP, AMAZ and F_{100} and F_{300} of PFAT from Tab. 1.

To test the emission feedbacks in 2100 and 2300 of PFAT, we generate 10 equally spaced values of F_{100} and F_{300}, covering the whole uncertainty range and 10 equally spaced values of P, also covering the respective uncertainty range. With this parameter set, we generate 100 model runs, one for each combination of pairs of F_{100} and F_{300} and P. CTEM is coupled to FaIR which is run with its default parameterization under SSP5-8.5, which has also been used for the calibration of CTEM. Now we calculate the difference between the cumulative carbon emissions from CTEM and the expected cumulative carbon emissions based on the values of F_{100} and F_{300} and T for the years 2100 and 2300. In 2100 there are significant deviations between the two, with the cumulative emissions of PFAT from CTEM being smaller than expected (Fig. S4). The relative error of the cumulative carbon emissions in 2100 increases with increasing values for P, whereas the value of F_{100} does not seem to have an effect on the error. Maximum errors of up to 80% are reached for the highest realization of P. Nevertheless, the relative error is reduced to values below 5% for all combinations of F_{300} and P in 2300. This implies that the medium H is too large to allow for high enough emissions between crossing the tipping point of PFAT and 2100. However, we regard this as the best possible implementation of PFAT since the long-term cumulative carbon emissions still roughly match the estimates and lower values of H would lead to potentially unrealistic abrupt carbon emissions.

For PFTP and AMAZ, we test how well the estimated values of H are met by CTEM for various combinations of K and P. We produce 10 equally spaced values of K and P, covering the whole uncertainty range and run the model for each combination for both PFTP and AMAZ, with all other TEs within CTEM being deactivated. In this manner, we produce 100 model runs for the minimum, the mean, and the maximum estimate of H for PFTP and AMAZ. FaIR is again run with its default parameterization under SSP5-8.5. The relative error in H of PFTP and AMAZ increases with increasing values for H, with CTEM producing smaller values of H than expected for low P and higher values for high P. (Fig. S3). Differences in K seem to have nearly no impact on the error in H for both AMAZ and PFTP. Notably, the relative errors in H are higher for AMAZ, with -27% and 45% being reached for the maximum estimate of H. For PFTP, the errors are more symmetric, lying between -19% and 19% for the maximum estimate of H. The change of sign of the errors around the mean value of P makes sense, as the mean value of P has been used for the calibration. The observed lower values of H for low P and higher values of H for high P can be explained by the rate-dependence of both TEs, with higher exceedance of P leading to faster tipping. As the increase of T slows down over time under SSP5-8.5 (Fig. S8), lower values of P lead to lower H and vice versa. Hence, the observed errors in H of PFTP and AMAZ from CTEM comply with the rate dependence of both TEs and are therefore regarded to be realistic.

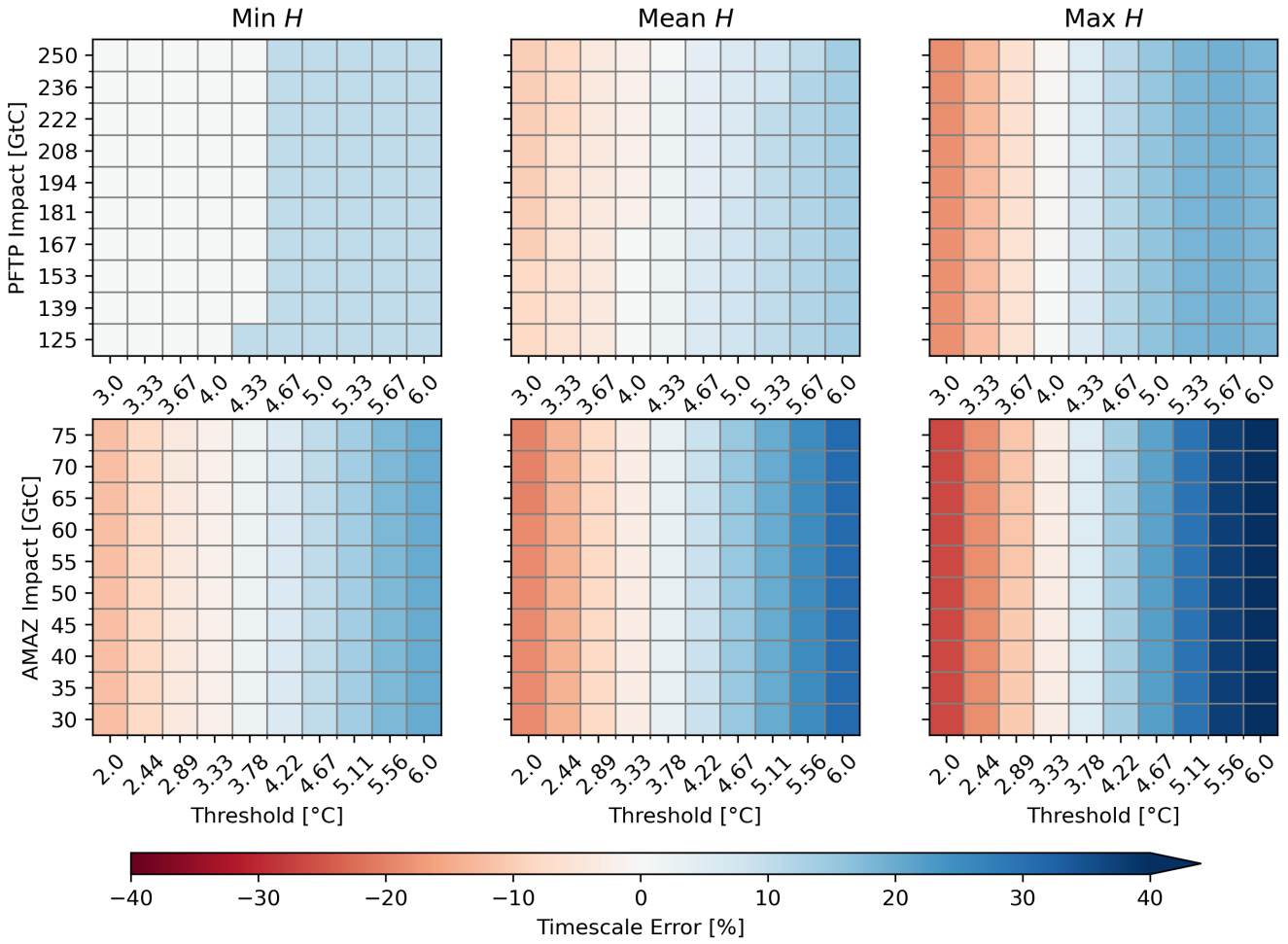

Figure S3. Deviations between the expected and the modelled H from CTEM in percent for the minimum, mean, and maximum estimate of H of PFTP and AMAZ with values of K and P equally spaced between the respective maximum and minimum estimate. One box represents one model realization with the respective values of P and K used for PFTP (upper row) or AMAZ (lower row) with all other TEs within CTEM being deactivated and FaIR run with default parametrization under SSP5-8.5.

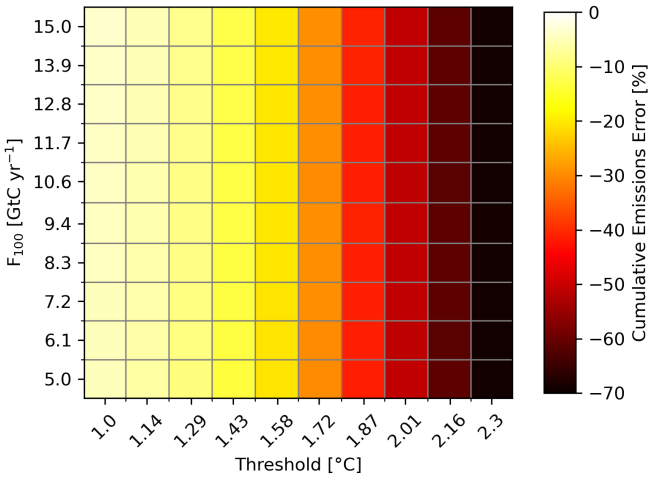

Figure S4. Deviations between the expected and the modelled cumulative carbon emissions from PFAT in 2100. One box represents one model realization with the respective values of P and F_{100} used for PFAT, with all other TEs within CTEM being deactivated and FaIR run with default parametrization under SSP5-8.5.

S5 Probability distributions used in CTEM

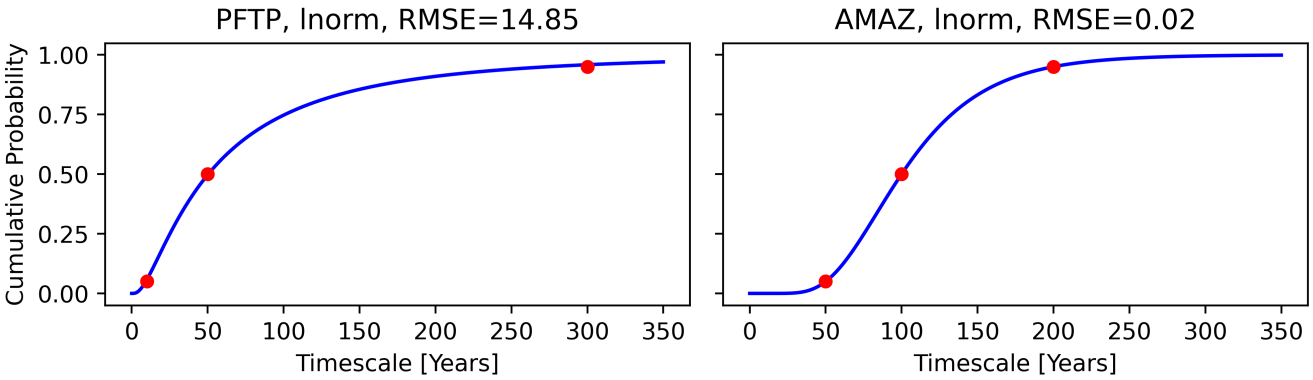

Figure S5. Cumulative distribution functions of H for PFTP and AMAZ, together with the RMSE between the given percentiles (red dots) and the actual percentiles of the respective distribution. The title states TE, distribution and RMSE in years.

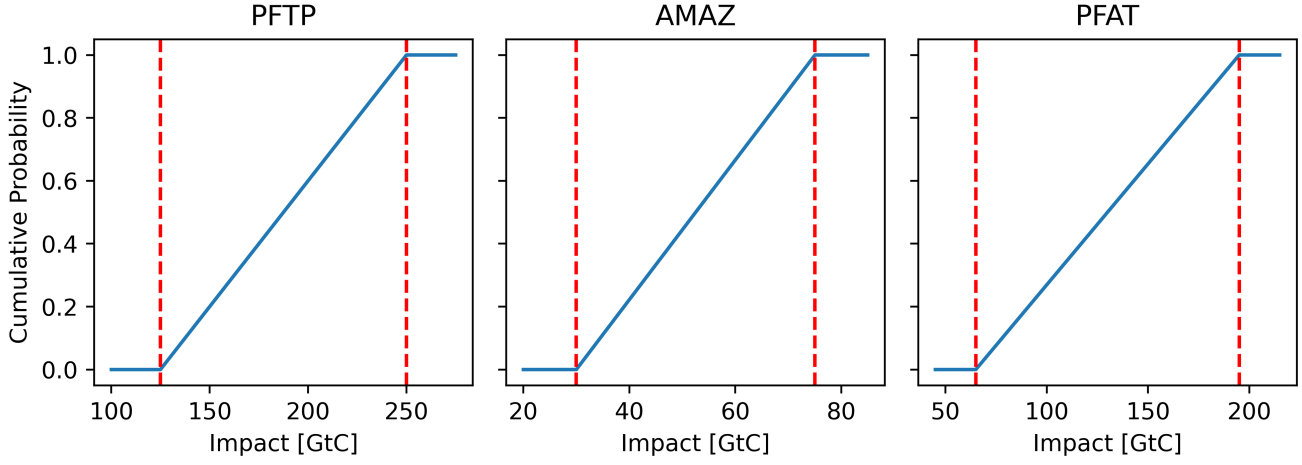

Figure S6. Cumulative distribution functions of K for AMAZ and PFTP and $K_{\max}$ for PFAT. The dotted red lines indicate the range of the respective variable from Tab. 1

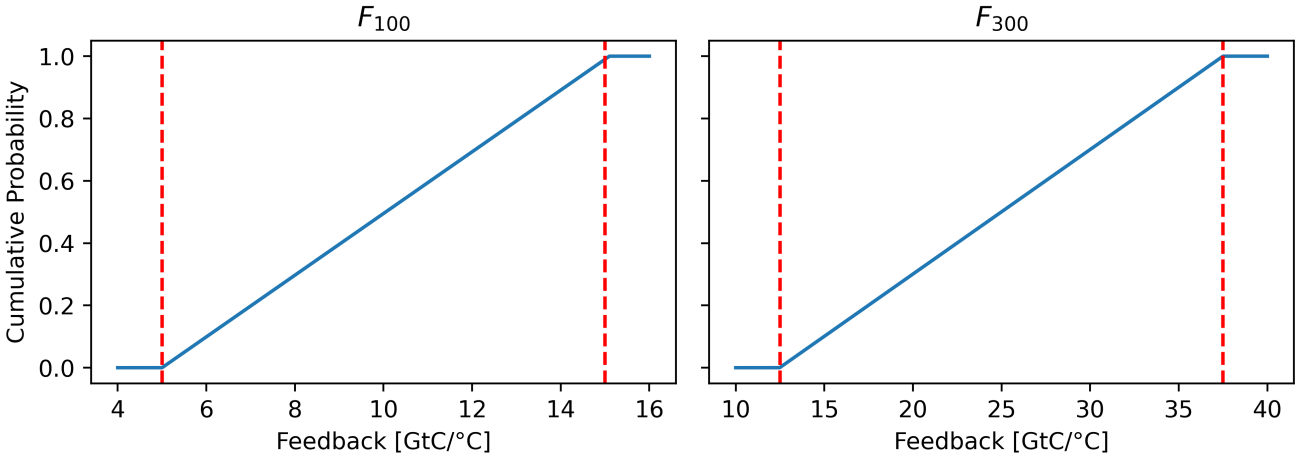

Figure S7. Cumulative distribution function of F_{100} and F_{300} of PFAT. The dotted red lines indicate the range of the respective variable from Tab. 1

S6 Why Prescribing Emissions from Carbon TEs Externally is Valid

To rule out possible double counting of carbon emissions from permafrost thaw or Amazon dieback, we have to make sure that these processes are not implicitly included in the parameters of FaIRv2.0.0. This could be the case if carbon emissions from both TEs and the respective warming were included either in the CMIP6 models used to parameterize the carbon cycle of FaIR or in the anthropogenic warming index distribution used to constrain this parameterization.

The CMIP6 data used for the parameterization of the FaIR carbon cycle is derived from the fully coupled and biogeochemical 1pctCO2 runs of eleven CMIP6 models (Arora et al., 2020). Of those eleven models, only two represent permafrost processes by including the effect of active layer thickening on decomposition of soil carbon (Canadell et al., 2021), which means they can represent PFGT but not PFAT or PFTP. Only three of those eleven CMIP6 models include vegetation dynamics (GFDL-ESM4, MPI-ESM1-2-LR and UKESM1-0-LL) and are therefore able to represent eventual dieback of AMAZ (Arora et al., 2020). Of those three, only GFDL-ESM4 predicts abrupt dieback in parts of AMAZ in the 1pctCO2 run, which, however, does not lead to significant reduction of the total carbon being stored in the Amazon vegetation (Parry et al., 2022). Therefore, we assume that carbon emissions from PFTP, PFAT and AMAZ are not implicitly included in the parameterization of the full parameter ensemble of FaIR.

If carbon emissions from AMAZ, PFTP or PFAT and the resulting global warming were already observable and detected in the dataset used to constrain the full parameter ensemble, the constrained parameter ensemble of FaIR would also account for those additional carbon emissions, as members with lower climate sensitivities were more likely to be excluded. However, no multi-decadal trend of $\mathrm{CO_2}$ or $\mathrm{CH_4}$ fluxes over the boreal permafrost region is yet detectable (Canadell et al., 2021), hence we assume that PFAT and PFTP carbon emissions are also not included in the constrained parameter ensemble of FaIR. Carbon emissions from AMAZ need to be considered more carefully, as the forest has already turned from a sink into a carbon source at the four measurement sites inspected by (Gatti et al., 2021). To get an impression of the potential magnitude of recent carbon emissions from AMAZ, we average over the four observed trends of total C flux ($0.2\ \mathrm{gCm^{-2}d^{-1}}$) and multiply this with the area of the forest of $7.25 \cdot 10^6\,\mathrm{km^2}$ (Gatti et al., 2021) and the days of the measurement period (2010–2018), which gives total emissions of 584 tC. Compared to the potential carbon emissions from AMAZ collapse of up to 75 GtC (Table 1), we regard this to be negligible and do assume that major contributions from AMAZ collapse are also not included in the constrained parameter ensemble of FaIR.

S7 Robustness of Ensemble Results

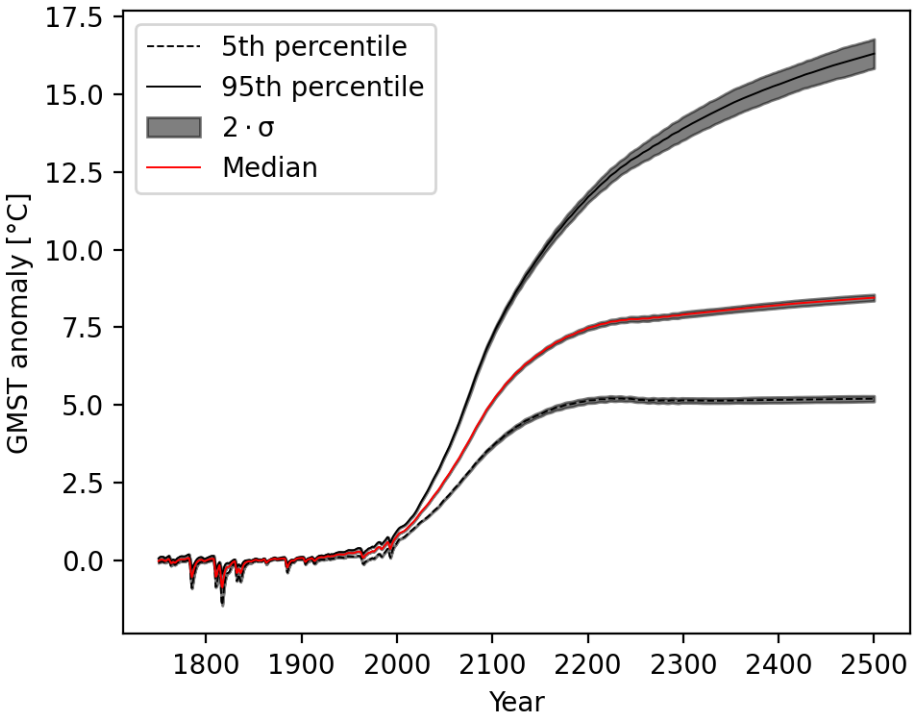

Figure S8. Comparison of the 5th percentile, the median and the 95th percentile of T between 20 coupled ensembles with 5000 members each. Mean estimate from all ensembles and two times standard deviation (σ) between the ensembles.

S8 Atmospheric Concentrations of Carbon Dioxide and Methane

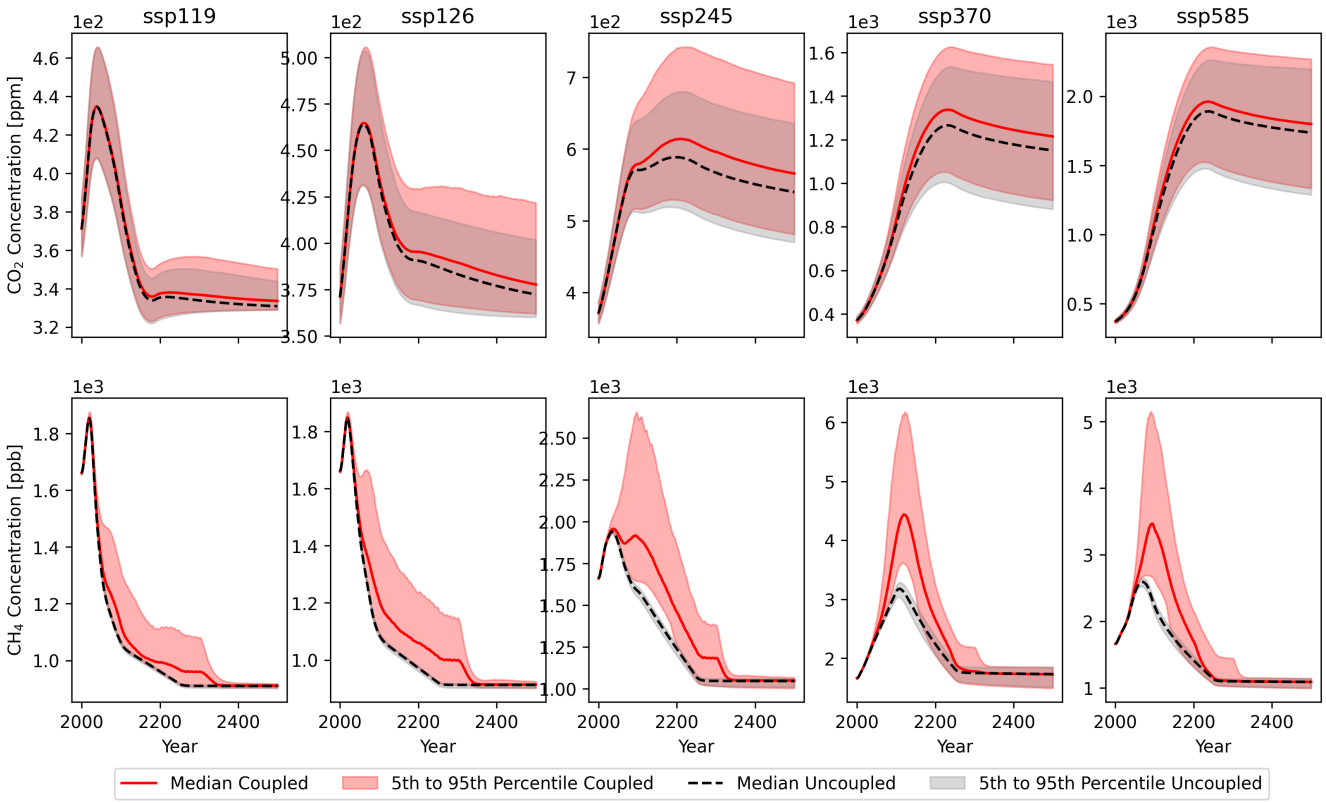

Figure S9. Atmospheric concentrations of CO_2 and CH_4 of the coupled and the uncoupled model ensemble for the five SSPs.

S9 Probabilities of Triggering Climate Tipping Elements

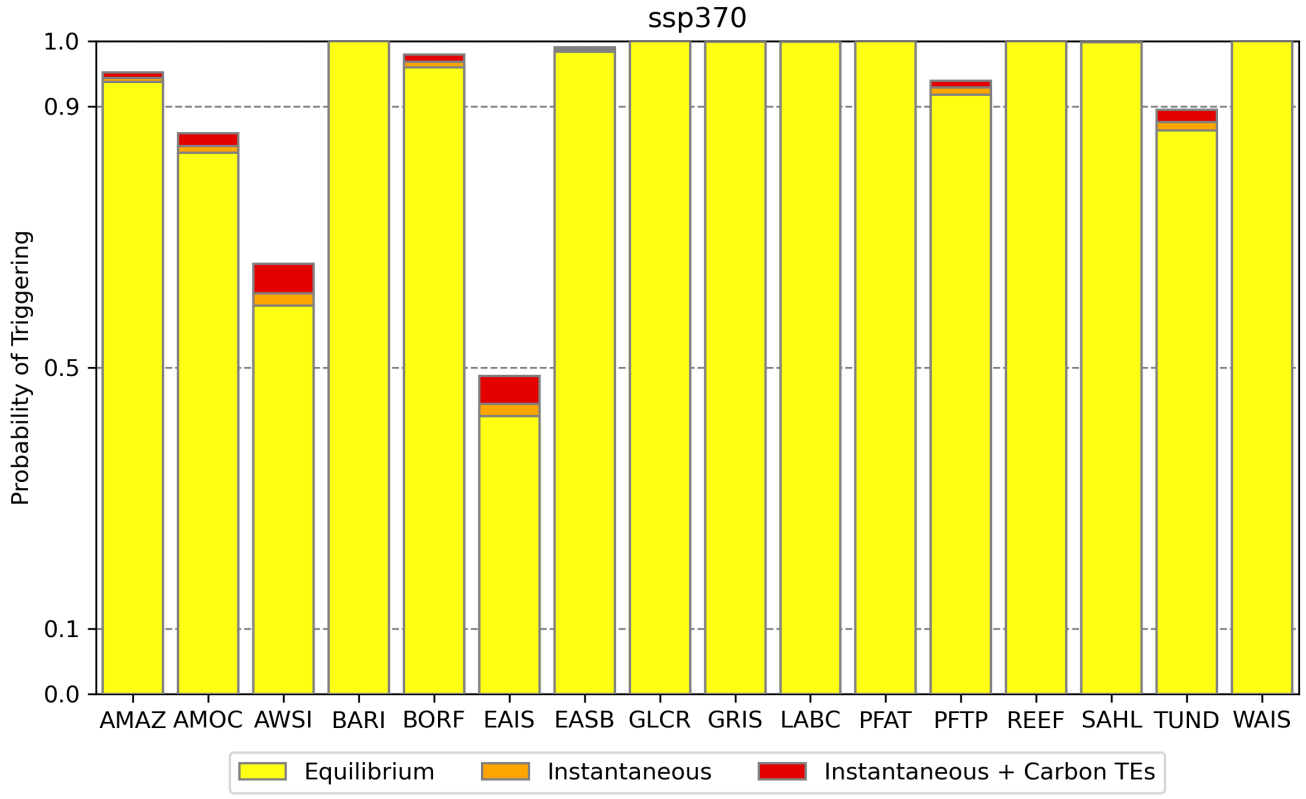

Figure S10. Probabilities of triggering the TEs by 2500 under SSP3-7.0 for the case of delayed triggering, instantaneous triggering and instantaneous triggering including the additional warming from carbon TEs.

References

Armstrong McKay, D. I., Staal, A., Abrams, J. F., Winkelmann, R., Sakschewski, B., Loriani, S., Fetzer, I., Cornell, S. E., Rockström, J., and Lenton, T. M.: Exceeding 1.5°C global warming could trigger multiple climate tipping points, Science (New York, N.Y.), 377, eabn7950, https://doi.org/10.1126/science.abn7950, 2022.

Arora, V. K., Katavouta, A., Williams, R. G., Jones, C. D., Brovkin, V., Friedlingstein, P., Schwinger, J., Bopp, L., Boucher, O., Cadule, P., Chamberlain, M. A., Christian, J. R., Delire, C., Fisher, A. R. A., Hajima, T., Ilyina, T., Joetzjer, E., Kawamiya, M., Koven, C. D., Krasting, J. P., Law, R. M., Lawrence, D. M., Lenton, A., Lindsay, K., Pongratz, J., Raddatz, T., Séférian, R., Tachiiri, K., Tjiputra, J. F., Wiltshire, A., Wu, T., and Ziehn, T.: Carbon-concentration and carbon-climate feedbacks in CMIP6 models and their comparison to CMIP5 models, Biogeosciences, 17, 4173–4222, https://doi.org/10.5194/bg-17-4173-2020, 2020.

Canadell, J., Monteiro, P., Costa, M., Cotrim da Cunha, L., Cox, P., Eliseev, A., Henson, S., Ishii, M., Jaccard, S., Koven, C., Lohila, A., Patra, P., Piao, S., Rogelj, J., Syampungani, S., Zaehle, S., and Zickfeld, K.: Global Carbon and other Biogeochemical Cycles and Feedbacks, p. 673–816, Cambridge University Press, Cambridge, United Kingdom and New York, NY, USA, https://doi.org/10.1017/9781009157896.007, 2021.

Gao, F. and Han, L.: Implementing the Nelder-Mead simplex algorithm with adaptive parameters, Computational Optimization and Applications, 51, 259–277, https://doi.org/10.1007/s10589-010-9329-3, 2012.

Gatti, L. V., Basso, L. S., Miller, J. B., Gloor, M., Gatti Domingues, L., Cassol, H. L., Tejada, G., Aragão, L. E., Nobre, C., Peters, W., Marani, L., Arai, E., Sanches, A. H., Corrêa, S. M., Anderson, L., Von Randow, C., Correia, C. S., Crispim, S. P., and Neves, R. A.: Amazonia as a carbon source linked to deforestation and climate change, Nature, 595, 388–393, https://doi.org/10.1038/s41586-021-03629-6, 2021.

Parry, I., Ritchie, P., and Cox, P.: Evidence of Amazon rainforest dieback in CMIP6 models, EGUsphere, pp. 1–11, http://arxiv.org/abs/2203.11744, 2022.